



Hydrogen Dimers in Giant-planet Infrared Spectra

Leigh N. Fletcher¹ , Magnus Gustafsson², and Glenn S. Orton³

¹ Department of Physics and Astronomy, University of Leicester, University Road, Leicester, LE1 7RH, UK; leigh.fletcher@le.ac.uk

² Applied Physics, Division of Materials Science, Department of Engineering Science and Mathematics, Luleå University of Technology, SE-97187 Luleå, Sweden

³ Jet Propulsion Laboratory, California Institute of Technology, 4800 Oak Grove Drive, Pasadena, CA 91109, USA

Received 2017 November 8; revised 2017 December 6; accepted 2017 December 6; published 2018 March 15

Abstract

Despite being one of the weakest dimers in nature, low-spectral-resolution *Voyager/IRIS* observations revealed the presence of $(\text{H}_2)_2$ dimers on Jupiter and Saturn in the 1980s. However, the collision-induced $\text{H}_2\text{--H}_2$ opacity databases widely used in planetary science have thus far only included free-to-free transitions and have neglected the contributions of dimers. Dimer spectra have both fine-scale structure near the S(0) and S(1) quadrupole lines (354 and 587 cm^{-1} , respectively), and broad continuum absorption contributions up to $\pm 50\text{ cm}^{-1}$ from the line centers. We develop a new ab initio model for the free-to-bound, bound-to-free, and bound-to-bound transitions of the hydrogen dimer for a range of temperatures ($40\text{--}400\text{ K}$) and para-hydrogen fractions ($0.25\text{--}1.0$). The model is validated against low-temperature laboratory experiments, and used to simulate the spectra of the giant planets. The new collision-induced opacity database permits high-resolution ($0.5\text{--}1.0\text{ cm}^{-1}$) spectral modeling of dimer spectra near S(0) and S(1) in both *Cassini* Composite Infrared Spectrometer observations of Jupiter and Saturn, and in *Spitzer* Infrared Spectrometer (IRS) observations of Uranus and Neptune for the first time. Furthermore, the model reproduces the dimer signatures observed in *Voyager/IRIS* data near S(0) on Jupiter and Saturn, and generally lowers the amount of para- H_2 (and the extent of disequilibrium) required to reproduce *IRIS* observations.

Key words: molecular data – planets and satellites: atmospheres – planets and satellites: gaseous planets – radiative transfer – techniques: spectroscopic

Supporting material: tar.gz file

1. Introduction

Far-infrared spectra of giant-planet atmospheres are dominated by continuum absorption resulting from collisions between molecular hydrogen and helium. This $\text{H}_2\text{--H}_2$ and $\text{H}_2\text{--He}$ collision-induced absorption (CIA) provides a thermometer to measure the thermal structure of the upper tropospheres of Jupiter, Saturn, Uranus, and Neptune (e.g., Conrath et al. 1998), and has been exploited by Earth-based astronomers, space observatories (e.g., *ISO*, *Spitzer*, *AKARI*, *Herschel*), and visiting spacecraft (e.g., *Voyager*, *Galileo*, and *Cassini*). The short-lived dipoles induced by these collisions between free molecules (*free-to-free* interactions) generate broad and smooth spectral features around the rotational S(0) (354 cm^{-1}) and S(1) (587 cm^{-1}) lines. Transitions between para- H_2 rotational levels $0 \rightarrow 2$ are responsible for the S(0) features (even rotational quantum numbers), and transitions between ortho- H_2 rotational levels $1 \rightarrow 3$ are responsible for the S(1) feature. Measurement of the far-infrared spectrum can therefore provide constraints on the tropospheric temperatures, para- H_2 fractions (a tracer of atmospheric mixing; Conrath et al. 1998), and the bulk helium abundance (Conrath & Gautier 2000).

It has been common practice to only include these free-to-free contributions when calculating the opacity of giant-planet atmospheres, in addition to the narrow quadrupole lines. However, sharp features near S(0) (354 cm^{-1}) identified in *Voyager IRIS* 4.3 cm^{-1} resolution spectra of Jupiter and Saturn were attributed to hydrogen dimers by Frommhold et al. (1984) and McKellar (1984), and confirmed via low-temperature experiments by McKellar (1988). This dimeric absorption, detectable as a slight modification to the free-free absorption of the parent molecules, is the result of the formation of a weakly

bound $(\text{H}_2)_2$ complex held together by van-der-Waals forces. The main mechanism of dimer formation and dissociation is three-body interactions, which sustain a dimer abundance determined by thermal equilibrium. To a much smaller extent, dimers may be formed during *free-to-bound* ($\text{H}_2 + \text{H}_2 \rightarrow (\text{H}_2)_2$) radiative transitions, which generate features redward (smaller wavenumbers) of the rotational line center in the absorption spectrum; and dissociated during *bound-to-free* transitions ($(\text{H}_2)_2 \rightarrow \text{H}_2 + \text{H}_2$), which generate spectral signatures blueward (larger wavenumbers) of the line center (e.g., from ab initio models by Frommhold et al. 1984). As the dimer lifetime is much longer than the short-lived free-to-free collisions, the spectral features are much narrower. Despite being one of the weakest dimers in nature, the $(\text{H}_2)_2$ contribution was readily visible in the *Voyager* spectra near S(0).

Following their identification, series of experimental and theoretical results were presented to characterize the dimer contributions (Schaefer 1987; McKellar 1988, 1990; McKellar & Schaefer 1991). The strength of the dimer absorption depends on the abundance of H_2 , the ortho-para ratio, and the temperature. The influence of the dimers on the spectrum is most important at low temperatures, as shown in the 20 K experiments by McKellar & Schaefer (1991). Meyer et al. (1989) demonstrated that the extra free-to-bound and bound-to-free transitions could alter the continuum tens of wavenumbers away from the line center. Carlson et al. (1992) fitted the Meyer calculations with empirical formulae to incorporate this broad-band dimer structure into the *IRIS* modeling, finding that this additional absorption significantly improved their fit near 350 cm^{-1} . Furthermore, Kim et al. (1995) and Trafton et al. (1997) identified dimer emission in Jupiter, Saturn, and Neptune near the H_2 fundamental at $2.1\text{ }\mu\text{m}$.

However, despite these pioneering studies, subsequent analyses over the past two decades have largely omitted this additional absorption and considered only the free-to-free transitions. Analyses of giant-planet infrared spectra have typically utilized the free-free $\text{H}_2\text{--H}_2$ opacity model of Borysow et al. (1985), which was based on ab initio dipole surfaces from Meyer et al. (1989). However, Orton et al. (2007) demonstrated that an error had been made in the modeling of the dipole components by Borysow et al. (1985), which appeared at the rotational double transitions in the absorption spectrum. Orton et al. (2007) carried out extensive corrected calculations, which were otherwise at the same level of theory as Borysow et al. (1985). Their corrected free-to-free coefficients, which were only provided (i) for normal H_2 (i.e., a 3:1 mixture of ortho- H_2 and para- H_2) and (ii) for H_2 with para and ortho states in equilibrium at the local temperature, now form the “Alternative” CIA database maintained by HITRAN (Richard et al. 2012). However, Fletcher et al. (2017) showed that this new free-to-free calculation resulted in smaller absorption coefficients near the S(0) and S(1) lines than the original database of Borysow et al. (1985), which led to spurious effects when fitting *Voyager/IRIS* spectra of Jupiter, despite being a more accurate calculation of the free-to-free contribution. The solution requires the addition of the dimer opacity, as originally envisaged by Frommhold et al. (1984), Carlson et al. (1992), and others. This was employed by Orton et al. (2014a) in their analysis of Uranus’ S(1) line from *Spitzer* data, which confirmed the existence of dimer features in Uranus’ far-infrared spectrum for the first time. In summary, use of the free-to-free absorption coefficients of Orton et al. (2007) in isolation will underestimate the opacity required to properly reproduce giant-planet spectra. Bound-to-free and free-to-bound absorption coefficients, calculated for a range of temperatures and para- H_2 fractions, are also required.

Section 2 presents new calculations of the free-to-free, bound-to-free, free-to-bound, and bound-to-bound ($(\text{H}_2)_2 \rightarrow (\text{H}_2)_2$) contributions to the $\text{H}_2\text{--H}_2$ opacity for giant-planet atmospheres, extending the work of Orton et al. (2007). Section 3 shows that the new ab initio model can be used to reproduce the fine-scale structure observed in high-resolution spectroscopy of the S(0) and S(1) regions on all four giant planets, using data from *Cassini* (Jupiter and Saturn) and *Spitzer* (Uranus and Neptune). We present the first observations of the S(0) dimer on Uranus; the first observation of both S(0) and S(1) dimers on Neptune; and the first observation of the S(1) dimers on Jupiter and Saturn. Inclusion of this structured dimer absorption along with the smooth CIA will be essential for interpretations of spectra from the *James Webb Space Telescope*.

2. Spectral Calculation

The quantum mechanical calculations of the interaction-induced spectra have been divided into three categories according to the physical mechanism, each category having its own method of calculation of the $\text{H}_2\text{--H}_2$ wavefunctions. The first two categories are also described briefly in Gustafsson (2017).

Free-to-free. This contribution is computed using the conventional method with an isotropic interaction potential (Meyer et al. 1989). The use of the isotropic potential approximation (IPA) is justified, as the anisotropy has been shown to have only a small effect on the absorption coefficient for $\text{H}_2\text{--H}_2$, in particular around the rotational transitions that we focus on in this work (Gustafsson et al. 2003; Karman et al. 2015). A

Numerov algorithm (Korn & Korn 1968) is implemented to obtain the one-dimensional continuum wavefunctions. The table presented by Orton et al. (2007) has been refined in the regions surrounding the S(0) and S(1) transitions, 310–400 cm^{-1} and 530–630 cm^{-1} , respectively, to account for the presence of fine features in the energy-dependent absorption cross section. These have to be resolved for an accurate numerical integration over energy, which is done to obtain the temperature-dependent absorption coefficient. Finally, we extend the work of Orton et al. (2007) by calculating the free-to-free absorption coefficients on a grid of 10 temperatures (40–400 K) and 10 para- H_2 fractions (0.25–1.0).

Bound-to-free and free-to-bound. Here the isotropic potential approximation (IPA) is also applied. The bound state wavefunctions are computed with a discrete variable representation (DVR) with a uniform grid (Colbert & Miller 1992) and the continuum states are computed with the Numerov algorithm. The formula for the absorption coefficient is taken from Meyer et al. (1989). A 0.5 cm^{-1} empirical shift of the upper dimer level was applied for the free-to-bound transitions on the low-frequency side of the S(0) line. The shift is applied for collisions where the H_2 molecules are in the $(j_1, j_2) = (0, 0)$, $(0, 1)$, or $(1, 0)$ rotational states. The shift was identified empirically via comparison with experimental data, but the magnitude is consistent with the comparison of these dimer levels (which are computed with the isotropic potential) with those computed using the full anisotropic potential, given below. For the upper dimer level the difference is on the order of 0.5 cm^{-1} .

Bound-to-bound. These calculations require the inclusion of the anisotropy of the potential to give transition frequencies in agreement with those observed in the laboratory. A new program, using the DVR algorithm with an anisotropic potential, was developed to compute the absorption coefficient. The method is outlined in the Appendix.

All calculations have been carried out using the potential by Schäfer & Köhler (1989) and the dipole by Meyer et al. (1989). A more recent potential surface, which was used by Karman et al. (2015), has also been tested, but it failed to give dimer states that are consistent with the experiments.

Figures 1–3 compare our calculated absorption spectra surrounding the S(0) and S(1) transitions with experimental data at temperatures of 20 K (McKellar & Schaefer 1991) and 77 K (McKellar 1988). A variety of para- to ortho-hydrogen ratios have been used in these figures. The computed bound-to-bound spectrum was convolved with a triangular slit function of width $w = 0.2 \text{ cm}^{-1}$ to match the experimental resolution. The sums of the spectral contributions agree reasonably well with the experiment. For the cases of pure para-hydrogen, the agreement is particularly good (Figures 1–2). For the case of equilibrium-hydrogen (Figure 3) the agreement is better for the S(0) transition than for the S(1) transition. This difference implies that the $j_i > 0$ monomer rotations are more poorly described in the bound-to-free and free-to-bound cases, indicating that an anisotropic potential treatment would improve the agreement. We also note that the density was higher for the experimental measurements taken with a larger fraction of ortho-hydrogen, so that pressure-broadening may have affected these spectral features.

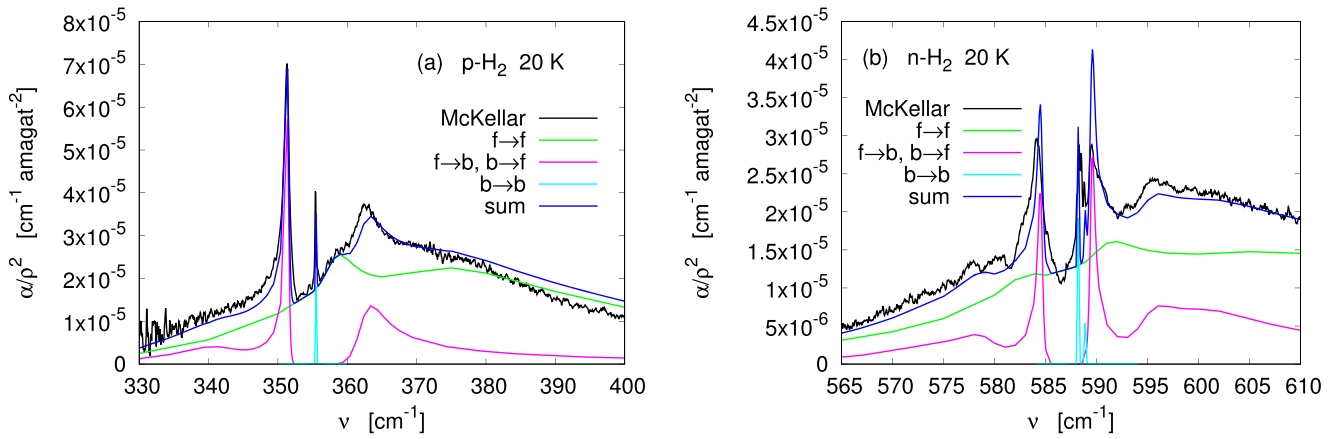


Figure 1. The absorption coefficient at 20 K, normalized by the square of the hydrogen density, around (a) the S(0) and (b) the S(1) transitions for pure para-hydrogen and for normal-hydrogen, respectively. The calculations are performed as described in Section 2. The line labeled “McKellar” represents the laboratory measurements by McKellar & Schaefer (1991). Pressures of about 49 Torr (equivalent to a density of 0.88 amagat) and 40 Torr (equivalent to a density of 0.72 amagat) were used in experiments in (a) and (b), respectively.

3. Giant-planet Modeling

3.1. Sources of Data

To date, the $(\text{H}_2)_2$ dimer absorption has only been studied near the S(0) feature in *Voyager/IRIS* 4.3 cm^{-1} resolution spectra of Jupiter and Saturn (Frommhold et al. 1984) and were identified in $R \sim 600$ resolution *Spitzer* spectra of the S(1) feature on Uranus (Orton et al. 2014a, although no attempts were made to fit the spectral features). We utilize *Cassini* Composite Infrared Spectrometer (CIRS, Flasar et al. 2004) spectra of Jupiter and Saturn with a wavenumber-independent 0.48 cm^{-1} spectral resolution, and *Spitzer* Infrared Spectrometer (IRS, Houck et al. 2004) wavelength-dependent $R \sim 600$ spectra of Uranus and Neptune (i.e., 0.59 cm^{-1} resolution at S(0) and 0.98 cm^{-1} resolution at S(1)). However, as the true spectral resolution of the high-resolution *Spitzer* modes is uncertain, we find that a resolution of 0.48 cm^{-1} is sufficient for our calculations.

Jupiter and Saturn. Spectra of the S(0) line were acquired by the far-IR polarizing CIRS focal plane one with its circular 4.3 mrad diameter field of view, whereas spectra of the S(1) line used the 0.273 mrad square detectors of CIRS focal plane 3. Given that the detector responsivities are low in these spectral regions, large numbers of spectra were coadded to generate a single average. We ensured that the footprints of the detectors were fully on the planetary disk, and that all spectra with emission angles smaller than 45° were averaged. For Jupiter, we averaged spectra spanning from 2000 November 15th to 2001 February 15th during the *Cassini* flyby—850 spectra were used for S(0), and 15,000 spectra were used for S(1). For Saturn, we averaged spectra from 2004 October to 2016 December with the same criteria, using 57,000 spectra for S(0) and 86,000 spectra for S(1). Although these large averages were necessary to improve the signal-to-noise, the resulting atmospheric profiles (temperature and para- H_2) are averaged over a broad region of the planet, and in the case of Saturn, over different seasons from southern summer to northern spring. As shown in Section 4 and Figure 4, these spectra reveal dimeric structure around S(0) on both planets, and tentatively around S(1) on Saturn.

Uranus and Neptune. *Spitzer/IRS* acquired $7\text{--}36 \mu\text{m}$ disk-integrated spectra of Uranus during Directors Discretionary Time on 2007 December 16–17, shortly after Uranus’ equinox

(program 467; full details of the data reduction process are provided by Orton et al. 2014a). Disk-integrated spectra of Neptune were acquired on 2005 November 19–20 during *Spitzer*’s Cycle 2 (program 20500), and reduced using the same process as Orton et al. (2014a). For both planets, the observations were designed to sample multiple longitudes during a complete rotation, but we averaged all longitudes to form a single spectrum. Here, we focus on high-resolution ($R \sim 600$) observations in the “Short-High” (SH) $9.95\text{--}19.30 \mu\text{m}$ and “Long High” (LH) $19.27\text{--}35.97 \mu\text{m}$ ranges, revealing the S(0) and S(1) lines in Figure 4, respectively. Note that Orton et al. (2014a) identified offsets between low-resolution and high-resolution Uranus spectra related to flux losses from different slit sizes, and ultimately scaled the SH data to match the low-resolution modes, and abandoned the LH data from their analysis entirely. In the present work, where only narrow spectral ranges are considered to identify the dimer features, we do not find it necessary to perform such a scaling and present good fits to both SH and LH data.

Voyager/IRIS: to supplement the high-resolution *Cassini* and *Spitzer* observations, we also reanalyze the low-resolution (4.3 cm^{-1}) *IRIS* observations of all four giant planets. These $180\text{--}2500 \text{ cm}^{-1}$ spectra were acquired by a Michelson interferometer in a series of north–south scans executed during the close flybys between 1979 and 1989. The selection criteria for the spectra and zonal averaging techniques have been previously described for Jupiter (Fletcher et al. 2017), Saturn (Fletcher et al. 2016), Uranus (Orton et al. 2015), and Neptune (Fletcher et al. 2014). Dimer features were previously identified only in the Jupiter and Saturn spectra (Frommhold et al. 1984), with the Uranus and Neptune data being too low in signal to reveal the dimer absorptions. The zonally averaged $300\text{--}550 \text{ cm}^{-1}$ regions of these spectra are re-analyzed with the new opacity database in Section 4.

3.2. Spectral Retrieval Model

The NEMESIS spectral retrieval algorithm (Irwin et al. 2008) was used to model the H_2 quadrupoles, dimers, and continuum absorption on all four giant planets in Figure 4. NEMESIS uses Newtonian iteration and an optimal estimation retrieval architecture (Rodgers 2000) to calculate planetary spectra, maximizing the quality of the spectral fit while using

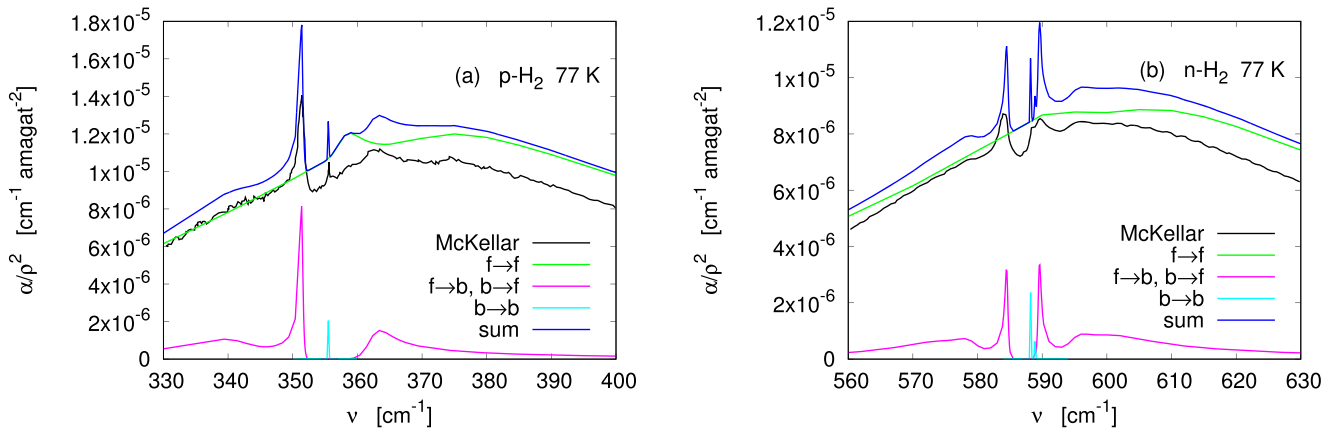


Figure 2. Same as Figure 1 but at a temperature of 77 K. In this case the laboratory measurements are from McKellar (1988) and were taken at number densities of 1.30 amagats and 2.45 amagats for (a) and (b), respectively.

constraints to prior data (in this case, vertical temperature and para-H₂ profiles) to ensure smooth and physically realistic retrieved profiles. For the spatially resolved spectra of Jupiter and Saturn, NEMESIS was used in its standard mode, computing spectra using the mean geometry (latitude and emission angle) of the spectral averages (e.g., Fletcher et al. 2009). For the disk-integrated Uranus and Neptune spectra, we employed an exponential-integral technique (Goody & Yung 1989) to compute the radiance into a hemisphere (Fletcher et al. 2014). Although the spectra explored in this paper are formed primarily by H₂, He (and H₂–CH₄ collisions, to a lesser extent), we use full atmospheric priors for each planet, including tropospheric (CH₄, PH₃, NH₃) and stratospheric species (hydrocarbons) based on previous NEMESIS studies of Jupiter and Saturn (Fletcher et al. 2009), Uranus (Orton et al. 2014a, 2014b), and Neptune (Fletcher et al. 2014). Although not strictly necessary in this analysis, the sources of spectral line data for these species are located in Table 4 of Fletcher et al. (2012).

The new ab initio model described in Section 2 produced calculations of the interaction-induced dimer spectra (free-to-bound, bound-to-free, bound-to-bound). This was combined with updated estimates of the free-to-free H₂–H₂ contribution, the H₂–He contribution from Borysow et al. (1988), and H₂–CH₄ and CH₄–CH₄ contributions from Borysow & Frommhold (1986, 1987). Extending the work of Orton et al. (2007), the new free-to-free H₂ and He contributions, as well as the dimer contributions, were calculated for a range of para-H₂ fractions between 0.25 and 1.0, and for temperatures from 40 to 400 K. These tables were then interpolated during the temperature and para-H₂ retrievals to calculate the atmospheric transmission. In addition, we included the H₂ quadrupole transitions from the ab initio calculations described in Rothman et al. (2013), which are in agreement with the recent experimental results of Campargue et al. (2012). Specifically, S(0) occurs at 354.3732 cm^{−1} with an intensity of 1.664×10^{-28} cm^{−1}/molec cm^{−2}; and S(1) occurs at 587.0320 cm^{−1} with an intensity of 2.657×10^{-27} cm^{−1}/molec cm^{−2}. Both have a width of 0.0017 cm^{−1}/atm (Reuter & Sirota 1994) and temperature dependence T^n , where $n=0.75$. Full vertical profiles of $T(p)$ and para-H₂ ($f_p(p)$) were retrieved independently to reproduce the eight spectral regions shown in Figure 4. Note that retrievals over a broader spectral range would be required to fully constrain these atmospheric profiles,

whereas the present study aims to show that the fine-scale dimeric structure can be adequately reproduced.

4. Results and Discussion

4.1. High-resolution Dimer Structure

Figure 4 compares model spectra to the high-resolution *Cassini* and *Spitzer* measurements in the regions within a few tens of wavenumbers of the quadrupole transitions. On Jupiter and Saturn, the CIRS data provided better signal-to-noise near the S(0) line than the S(1) line, permitting identification of the main free-to-bound (351.1 cm^{−1}, $l = 2 \rightarrow 1$) and bound-to-free (357 cm^{−1}, $l = 1 \rightarrow 2$) transitions ~ 3 cm^{−1} to either side of the quadrupole. These features are seen in absorption, as the strongest dimer absorptions are sensing higher, cooler altitudes near the tropopause on both planets. The asymmetry in the line intensities between these two features (shown in Figures 1–3 for the S(0) line) is related to the boson symmetry of para-H₂ (Frommhold et al. 1984). Additional undulations in the continuum can be seen near 346 cm^{−1} and 363 cm^{−1} (free-to-bound $l = 3 \rightarrow 0$ and bound-to-free $l = 0 \rightarrow 3$, respectively) that contribute to the overall absorption provided by the broad free–free transition. Although these gas-giant S(0) dimers have been previously studied at low resolutions from *Voyager/IRIS* (see Section 4.2, Frommhold et al. 1984; McKellar 1984), this is the first observation at a sufficient spectral resolution to resolve their line shapes.

The CIRS observations near 587 cm^{−1} have much poorer noise characteristics near the edge of the detector responsivity curve, so little is identifiable beyond the central quadrupole lines. Figures 4(e)–(f) show that the expected dimer structure is within the uncertainty on the measurement, but we expect Jovian absorption and Saturnian emission near 584.5 cm^{−1} and 589.5 cm^{−1}, ~ 2.5 cm^{−1} to either side of the quadrupole emission. Saturn’s S(1) dimer appears in emission rather than absorption because it senses altitudes just above the tropopause, in the region where temperature begins to increase with altitude in the lower stratosphere.

The general appearance of the dimer absorption near S(0) changes character considerably for Uranus and Neptune, where both the data and model indicate that the main free-to-bound and bound-to-free transitions ~ 3 cm^{−1} from the line center are sensing stratospheric altitudes, warmer than the surrounding free–free transitions. The 351 cm^{−1} feature almost matches the

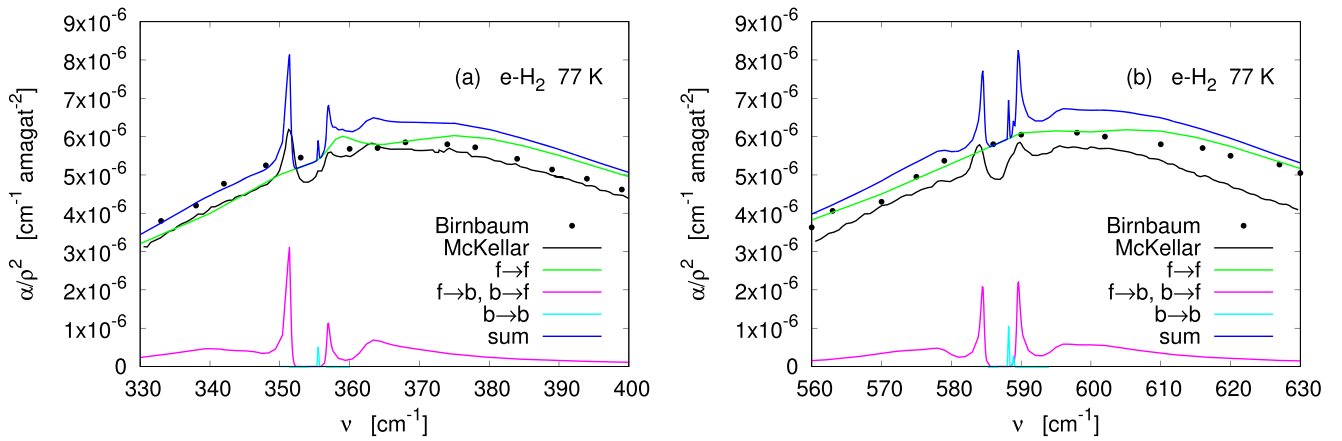


Figure 3. Same as Figure 2 but with equilibrium-hydrogen in both (a) and (b). The laboratory measurement by McKellar (1988) was taken at a number density of 2.63 amagats. Additional low-resolution laboratory measurements by Birnbaum (1978) are also included (circles), but these do not resolve the dimer features. However, this confirms that the overall magnitude of the calculated absorption is consistent with the experimental measurements.

intensity of the quadrupole line itself. The measured spectrum becomes increasingly noisy shortward of 347 cm^{-1} due to an overlap of modes in the *Spitzer* LH setting. However, this cannot account for the extremely poor fit to the spectrum between 352 and 354 cm^{-1} , where no dimer transitions exist to add to the absorption of the free-free contribution. The data suggest that excess absorption could be required to make the spectrum sense higher, cooler altitudes toward the tropopause, but experiments with ad hoc modifications to the dimer database failed to offer improvements. Given that there is no evidence of excess absorption in the gas-giant spectra, and that there are additional deviations in the *Spitzer* ice-giant measurements that are not accounted for by our model, it is likely that this mismatch is unrelated to the dimer spectra and is simply the result of noisy data. New measurements of the dimer features with *JWST* (see Section 5) or other far-IR facilities such as *SOFIA* should help to resolve this conundrum.

Ice-giant dimer features near S(1) are significantly weaker, owing to the quasi-isothermal tropopause regions to which the dimers are sensitive. Uranus' S(1) dimers were first identified by Orton et al. (2014a), but no attempt was made to fit the discrete structures. In Figure 4(g), the free-to-bound transition near 584.5 cm^{-1} is present in the data, but our model struggles to fit it due to the weakness of the bound-to-free transition near 589.5 cm^{-1} (the spectral fit is a compromise over fitting the whole region). The signal-to-noise ratio of the *Spitzer* data is excellent here, so this could represent a deficiency of the model. However, the model is more successful at fitting Neptune's S(1) line and dimer structure, which is stronger than that for Uranus and shows equal strength in the free-to-bound and bound-to-free transitions. We conclude that the new ab initio model provides adequate spectral fits to S(0) and S(1) features on all four giant planets, despite some model-data discrepancies that we hope to constrain with improved future measurements.

Finally, we note that two spectral models are shown in Figure 4—one without bound-to-bound transitions (red) and one with them (blue). Although the bound-to-bound transitions were clearly present in the experimental data (Figures 1–3), their influence near S(1) is negligible, and their importance on the giant-planet S(0) spectra is unclear. On Jupiter, the addition of the bound-bound opacity does improve the fit near 355.5 cm^{-1} . However, on Saturn, Uranus, and Neptune, the inclusion of the bound-bound data actually worsens the fits.

We have chosen to show both options, although the requirement for the bound-bound contribution remains unclear.

4.2. Low-resolution: *Voyager/IRIS*

Spectral modeling of *Voyager/IRIS* $300\text{--}550\text{ cm}^{-1}$ spectra of Jupiter by Fletcher et al. (2017) revealed a problem when the free-to-free transitions of Orton et al. (2007) were used in isolation, as they underpredicted the amount of collision-induced opacity required to fit the data with a physically plausible atmospheric structure. This present study was prompted by the need to add dimer opacity to the free-free continuum to explain the *Voyager* data. Ironically, the error in the calculation of some of the free-free components by Borysow et al. (1985) led to an opacity data set that was closer to reality. We repeat the *Voyager/IRIS* fitting using three assumptions for the $\text{H}_2\text{--H}_2$ opacity: (i) the original free-free database of Borysow et al. (1985), (ii) the newer free-free database of Orton et al. (2007), and (iii) the complete free-to-free, free-to-bound, bound-to-free, and bound-to-bound database of this work.

The quality of the *IRIS* spectral fits using the latter database is shown for all four planets in Figure 5. For the purpose of this plot, we averaged all *Voyager-1 IRIS* Jupiter and Saturn spectra within $\pm 30^\circ$ latitude of the equator, whereas for Uranus and Neptune we averaged all available *Voyager-2 IRIS* spectra from pole to pole, filtering for any corrupted measurements. Dimer features near S(0) are clearly identifiable and well-reproduced for Jupiter and Saturn (Frommhold et al. 1984), but are indistinguishable above the *IRIS* noise for Uranus and Neptune.

Figure 6 shows the consequences of using the three different CIA databases on retrievals of temperature and para- H_2 (f_p) from *Voyager IRIS* Jupiter spectra. As shown in Fletcher et al. (2017), the use of the free-free continuum of Orton et al. (2007; Figure 6(c)), without the additional absorption from the dimers near the S(0) and S(1) peaks, results in temperature retrievals with sharp lapse rates and low temperatures ($T < 106\text{ K}$) near the tropopause. In addition, the para- H_2 fraction is larger ($f_p = 0.33\text{--}0.34$), as the spectral model attempted to increase the radiance at 350 cm^{-1} by increasing the f_p , resulting in a strongly sub-equilibrium atmosphere (i.e., para- H_2 exceeds that expected from equilibrium). The goodness-of-fit was also significantly worse in the free-free case, by a factor of three. Note that we detected a 0.9 cm^{-1} offset

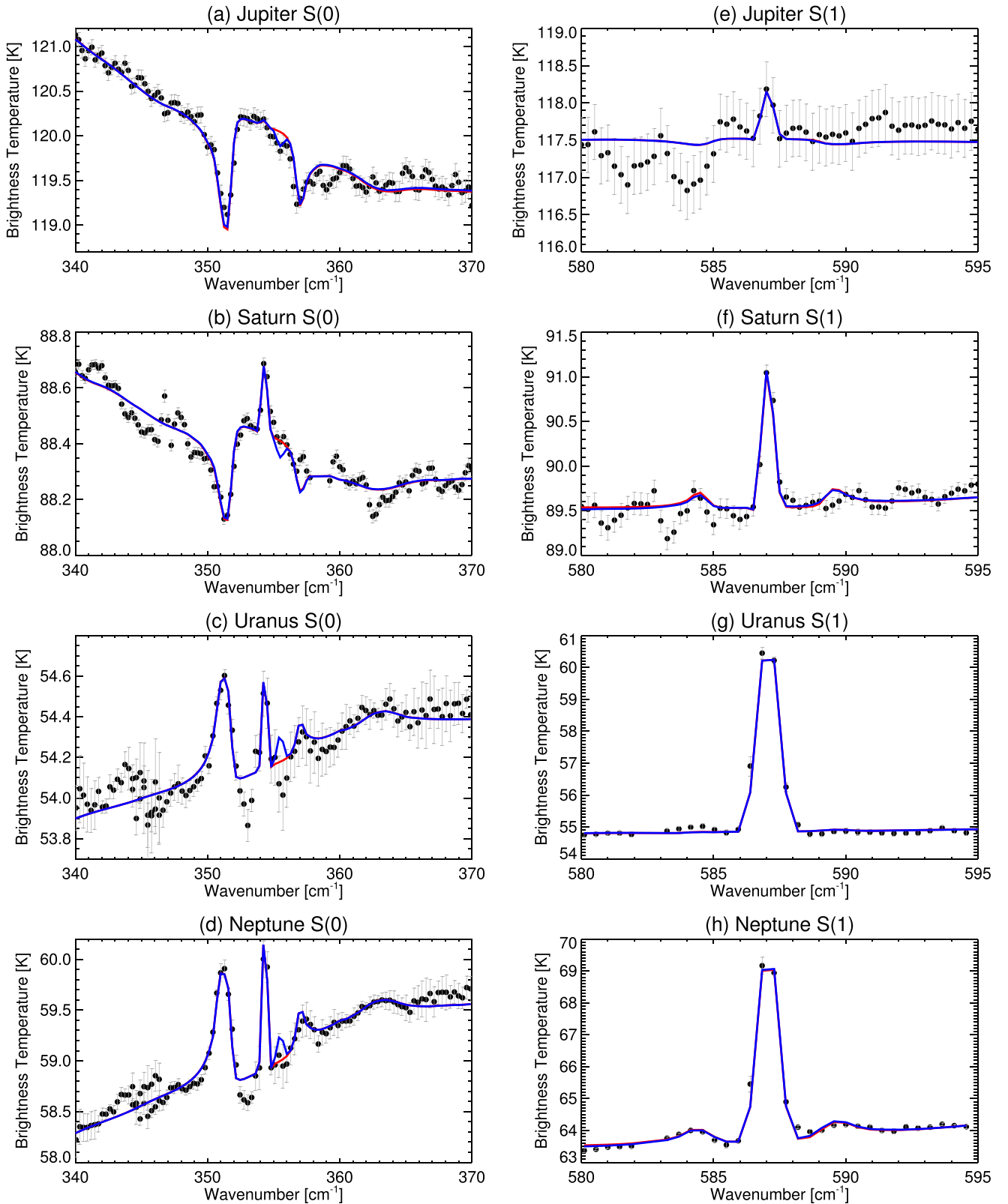


Figure 4. Spectral fits to the S(0) and S(1) lines detected on all four giant planets, using *Cassini* data for Jupiter and Saturn and *Spitzer* data for Uranus and Neptune.

between our spectral model and the *Voyager-1* *IRIS* Jupiter data (which was also present in the analysis of Fletcher et al. 2017), which was not present in the *Cassini* and *Spitzer* comparisons. The *IRIS* data in Figure 5 have been shifted in wavenumber to compensate. With the new dimer database, the retrieved

tropospheric temperatures are smoother, with a minimum $T \sim 110$ K and slightly lower $f_p = 0.32\text{--}0.33$, leading to para- H_2 conditions closer to equilibrium (albeit perturbed by equatorial upwelling and polar subsidence, as described by Conrath et al. 1998; Fletcher et al. 2017). This comes close to

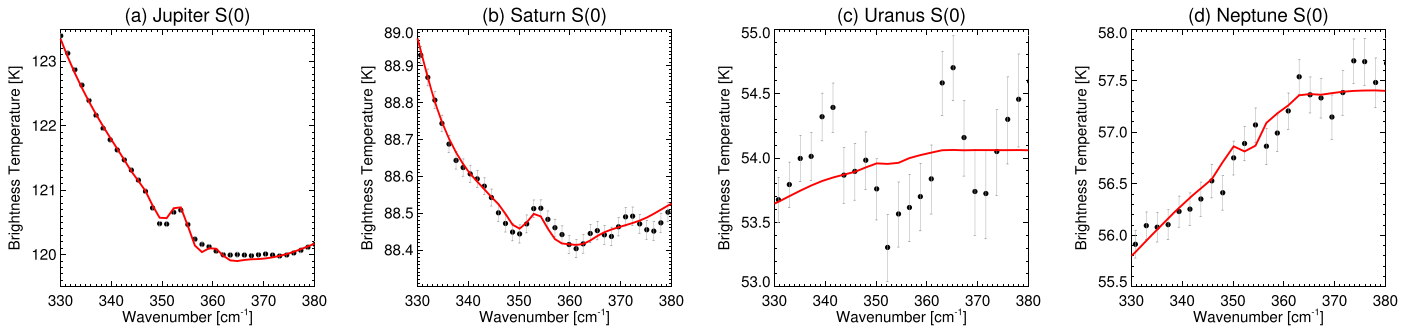


Figure 5. Large averages of *Voyager IRIS* spectra (black circles with standard errors on the mean) compared to the spectral model with all dimer transitions included (red line). Dimer absorption is clearly visible for Jupiter and Saturn observations, whereas the features are indistinguishable above the noise for Uranus and Neptune.

matching the calculations using the original database of Borysow et al. (1985), where some of the free-free components had been overestimated.

The same exercise was repeated for the *IRIS* Saturn data (Fletcher et al. 2016). Although the temperatures retrieved using the three compilations were similar (within ~ 1 K), the para- H_2 fraction altered by ~ 0.03 in the upper troposphere. As was the case for Jupiter, this caused the calculation with only the free-free database of Orton et al. (2007) to appear strongly sub-equilibrium (i.e., more para- H_2 required to increase the absorption near $S(0)$), whereas the dimeric absorption fulfills this role in our new calculation, bringing the atmosphere closer to equilibrium, albeit with seasonal north-south gradients in Saturn’s para- H_2 , as described by Fletcher et al. (2016). For Uranus and Neptune, where only the 200–400 cm^{-1} offer any constraint (and there is no sensitivity to the $S(1)$ at all), the differences in the retrieved temperatures and para- H_2 were negligible and the dimer structure near 354 cm^{-1} was not visible in the *Voyager/IRIS* 4.3 cm^{-1} resolution data (Figures 5(c)–(d)).

5. Conclusions

The purely free-to-free H_2-H_2 collision-induced absorption tables of Orton et al. (2007), which are included in the “Alternate” directory of HITRAN 2012 (Richard et al. 2012), should not be used in isolation when fitting mid- and far-infrared spectra in the vicinity of the $S(0)$ and $S(1)$ lines. Instead, we propose that they should be combined with the present refined opacity offered by free-to-free, free-to-bound, bound-to-free, and bound-to-bound H_2-H_2 transitions within ± 50 cm^{-1} of the line centers. A new *ab initio* model, using the isotropic interaction potential approximation and a denser energy grid than previous studies, is used to calculate the opacity provided by the former three types of transitions for a range of temperatures and para- H_2 fractions. Similarly, the opacity contribution from bound-to-bound transitions is computed with the full anisotropic interaction potential. This model is validated via comparison to laboratory measurements at 20 and 77 K (McKellar 1988; McKellar & Schaefer 1991), and then used in radiative transfer calculations to simulate the spectra of the four giant planets.

We find that we can reproduce the low-resolution (4.3 cm^{-1}) dimer signatures that had been previously identified in Jupiter and Saturn *Voyager* spectra by McKellar (1984), and that the additional continuum absorption resolves the problems that were identified by Fletcher et al. (2017) when using the free-free calculations of Orton et al. (2007) in isolation. Observations

at higher spectral resolutions (0.5–1.0 cm^{-1}) were compiled from *Cassini* CIRS observations of Jupiter and Saturn and *Spitzer* Infrared Spectrometer (IRS) observations of Uranus and Neptune. The model-data comparison reveals the presence of dimer absorption near $S(0)$ on all four planets at high spectral resolution, and near $S(1)$ on Uranus and Neptune (the structure is lost in the data uncertainty on Jupiter and Saturn). Dimeric transitions appear in absorption on the gas giants, where they sense the upper troposphere, and in emission on the ice giants, where they sense the lower stratosphere.

Fits to the data are adequate but not perfect. For example, the importance of bound-to-bound transitions is unclear, as they improve the fit for Jupiter but not for the other giant planets. Second, both Uranus and Neptune have model-data discrepancies between the quadrupole at 354.5 cm^{-1} and the primary dimer feature at 351 cm^{-1} that we cannot account for using the *ab initio* model. Note that the spectral calculations described in this work account only for binary interactions (between two hydrogen molecules), and not ternary or higher-order interactions. The sharp dimer features correspond to quantum states that are rather long-lived, and thus may be sensitive to these additional interactions, which is a possible source of error in the present modeling work. Currently, ternary and higher-order interactions cannot be treated well with quantum mechanics, which would be necessary in the case of hydrogen. One has to resort to classical mechanical treatments (see, e.g., Hartmann et al. 2011; Fakhardji & Gustafsson 2017), which are typically well-suited for higher-mass molecules such as CO_2 or N_2 . Nevertheless, the binary theory and isotropic potential approximation are able to reproduce much of the fine-scale structure observed in the giant-planet spectra presented in this work.

It is possible that better observational data, with a higher sensitivity and spectral sampling, will help resolve these discrepancies. The *James Webb Space Telescope*, when it launches in 2019, will provide exquisite spectral capabilities in the 5–30 μm range using the MIRI integral field units (Wells et al. 2015). Unfortunately, the collision-induced continua from Jupiter and Saturn are likely to cause detector saturation (although wavelengths shortward of 11 and 16 μm are likely to be accessible on Jupiter and Saturn, respectively). However, no saturation is expected for Uranus and Neptune, where both $S(0)$ and $S(1)$ will be available for further study at spectral resolutions of $R \sim 3000$ (channel 3LONG, 15.4–18.1 μm) and $R \sim 1600$ (channel 4LONG, 24.0–28.5 μm). Observations of all four giant planets are scheduled as part of the Guaranteed Time Program of H. Hammel and will provide an excellent test of the new dimer spectra provided in this study. Finally, given

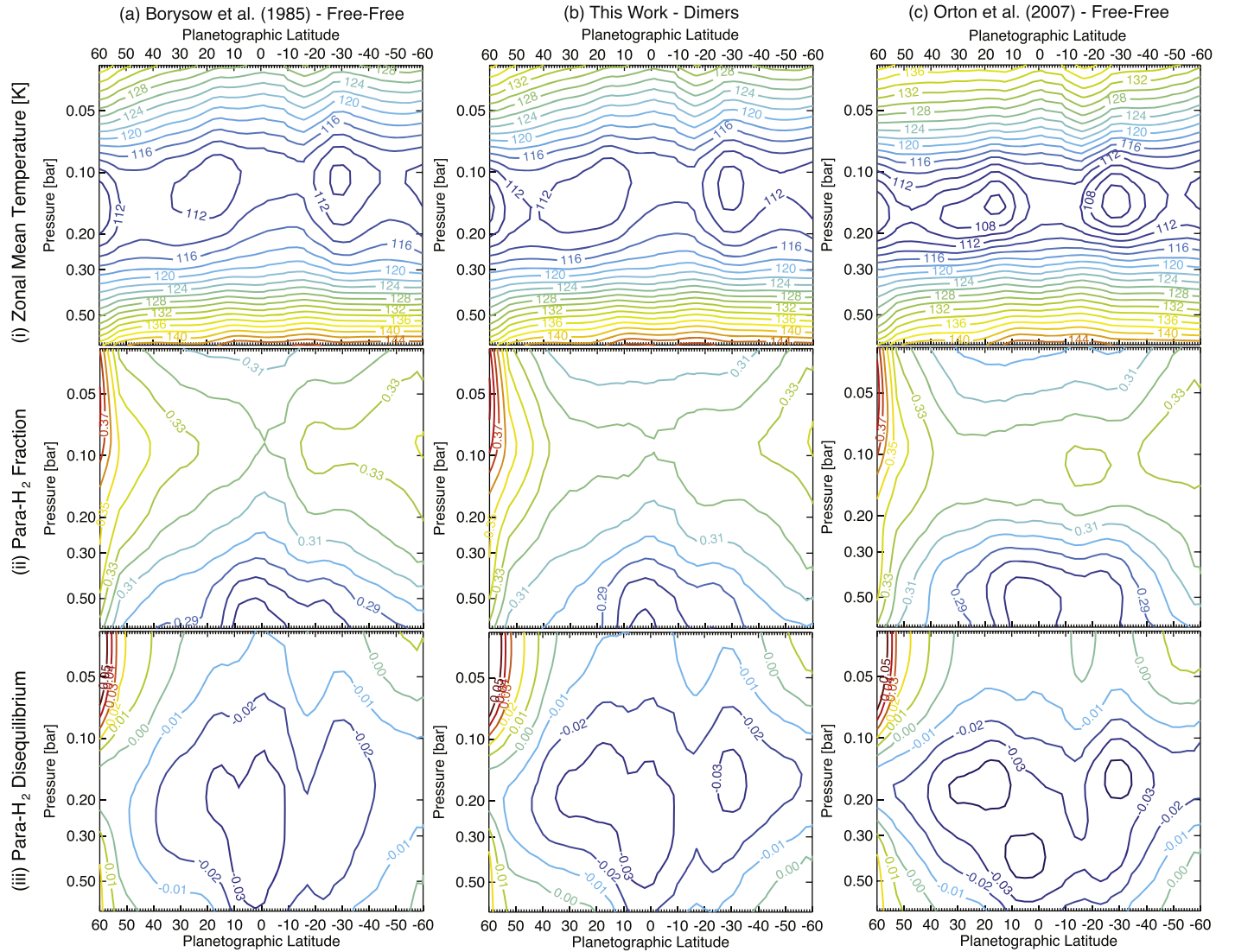


Figure 6. Comparison of retrieved (i) tropospheric temperatures; (ii) para-H₂ fraction; and (iii) difference between para-H₂ and equilibrium. More negative values in the bottom row indicate more para-H₂ than expected from equilibrium (i.e., sub-equilibrium conditions), potentially associated with upwelling motions. The results are compared between calculations using (a) the free-free continuum absorption of Borysow et al. (1985), (b) the new compilation with dimer absorption; and (c) the free-free continuum absorption of Orton et al. (2007).

the importance of this spectral range in determining the helium abundances on the giant planets via remote sensing (e.g., Conrath & Gautier 2000), we hope that this new dimer spectral database will be of use to the wider community.

L.N. Fletcher was supported by a Royal Society Research Fellowship and European Research Council Consolidator Grant (under the European Union’s Horizon 2020 research and innovation programme, grant agreement No 723890) at the University of Leicester. M. Gustafsson acknowledges support from the Knut and Alice Wallenberg Foundation. G. Orton was supported by funding from the National Aeronautics and Space Administration to the Jet Propulsion Laboratory, California Institute of Technology. The new free-to-free, free-to-bound, bound-to-free, and bound-to-bound opacity tables are all available at <https://github.com/leighfletcher/hydrogendimers>, [10.5281/zenodo.1095503](https://doi.org/10.5281/zenodo.1095503), and also in a .tar.gz package with this article.

Facilities: Cassini, Spitzer, Voyager.

Appendix Bound-to-bound Spectra

The bound states are computed with a discrete variable representation on a uniform grid (Colbert & Miller 1992). The formulas outlined below are for the case of two distinguishable hydrogen molecules, i.e., a complex consisting of one para-H₂ and one ortho-H₂. At the end we will describe the modifications needed to treat a complex consisting of two identical hydrogen molecules. We will also consider the hydrogen molecules as rigid rotors, as they are throughout this work. Under those conditions the Hamiltonian for two hydrogen molecules, with centers of mass separated by the vector \mathbf{R} , is:

$$H(\hat{\mathbf{r}}_1, \hat{\mathbf{r}}_2, \mathbf{R}) = H^{\text{mol}}(\hat{\mathbf{r}}_1) + H^{\text{mol}}(\hat{\mathbf{r}}_2) - \frac{\hbar^2}{2m} \nabla_{\mathbf{R}}^2 + V(\hat{\mathbf{r}}_1, \hat{\mathbf{r}}_2, \mathbf{R}), \quad (1)$$

where the orientations of the two diatoms are given by the unit vectors $\hat{\mathbf{r}}_1$ and $\hat{\mathbf{r}}_2$. V is the interaction potential and m is the

bimolecular reduced mass. The wavefunction is expanded in angular basis functions according to

$$\Psi_{JM}(\hat{\mathbf{r}}_1, \hat{\mathbf{r}}_2, \mathbf{R}) = \sum_{\beta} \frac{1}{R} F_{\beta}^J(R) Y_{j_1 j_2 j l}^{JM}(\hat{\mathbf{r}}_1, \hat{\mathbf{r}}_2, \hat{\mathbf{R}}), \quad (2)$$

where β is shorthand for the quantum numbers $(j_1 j_2 j l)$ and $Y_{j_1 j_2 j l}^{JM}$ is the vector coupling function:

$$\begin{aligned} Y_{j_1 j_2 j l}^{JM}(\hat{\mathbf{r}}_1, \hat{\mathbf{r}}_2, \hat{\mathbf{R}}) \\ = \sum_{m_1 m_2 m_j m_l} C(j_1, j_2, j; m_1, m_2, m_j) C(j, l, J; m_j, m_l, M) \\ \times Y_{j_1 m_1}(\hat{\mathbf{r}}_1) Y_{j_2 m_2}(\hat{\mathbf{r}}_2) Y_{l m_l}(\hat{\mathbf{R}}), \end{aligned} \quad (3)$$

corresponding to $\mathbf{J} = \mathbf{j} + \mathbf{l}$ and $\mathbf{j} = \mathbf{j}_1 + \mathbf{j}_2$. The angular momentum quantum numbers j_1 and j_2 correspond to the diatomic rotations, and l and J are the end-over-end and total angular momenta, respectively. The factors C are Clebsch–Gordan coefficients. The potential is also expanded in spherical harmonics, as in Gustafsson et al. (2003), and then the expansion (2) and the Hamiltonian (1) yield the DVR-matrix Hamiltonian:

$$\begin{aligned} H_{\alpha\alpha'\beta\beta'}^J = & \left(E_{j_1}^{\text{mol}} + E_{j_2}^{\text{mol}} + \frac{\hbar^2 l(l+1)}{2mR_{\alpha}^2} \right) \delta_{\alpha\alpha'} \delta_{\beta\beta'} \\ & + T_{\alpha\alpha'} \delta_{\beta\beta'} + V_{\beta\beta'}^J(R_{\alpha}) \delta_{\alpha\alpha'}, \end{aligned} \quad (4)$$

with the kinetic energy matrix:

$$T_{\alpha\alpha'} = \frac{\hbar^2}{2m \Delta R^2} (-1)^{\alpha-\alpha'} \begin{cases} \frac{\pi^2}{3} - \frac{1}{2\alpha^2} & \alpha = \alpha' \\ \frac{2}{(\alpha-\alpha')^2} - \frac{2}{(\alpha+\alpha')^2} & \alpha \neq \alpha' \end{cases}, \quad (5)$$

where the uniform DVR grid has a spacing $\Delta R = (R_{\text{max}} - R_{\text{min}})/N$ and corresponding grid points: $R_{\alpha} = R_{\text{min}} + \alpha \cdot \Delta R$ where $\alpha = 1, 2, \dots, (N-1)$. The Hamiltonian in Equation (4) is independent of the quantum number M (Green 1975) and thus the eigenvectors and eigenenergies are also M -independent. The H_2 rotational energies $E_{j_i}^{\text{mol}}$ are taken from Stoicheff (1957) and are shifted so that $E_0^{\text{mol}} = 0$. The potential matrix element is:

$$V_{\beta\beta'}^J(R_{\alpha}) = \sum_{\gamma_1 \gamma_2 \gamma} V_{\gamma_1 \gamma_2 \gamma}(R_{\alpha}) e_{\gamma_1 \gamma_2 \gamma}(j_1, j_2, j, l, j_1', j_2', j', l'; J), \quad (6)$$

where the coefficient, $e_{\gamma_1 \gamma_2 \gamma}$, and the expansion of V is given in Gustafsson et al. (2003). The Schrödinger equation is solved through diagonalization of the Hamiltonian (4) and $(N-1)N_{\beta}$ eigenvectors, $F_{\beta k}^J(R_{\alpha})$, and eigenenergies, E_k^J are obtained. N_{β} is the number of angular momentum basis functions in the expansion, Equation (2). The diagonalization is done with the DSYEV routine from LAPACK (Anderson et al. 1999).

With the eigenstates determined as described above, the absorption coefficient can be computed from the matrix elements of the interaction-induced electric dipole moment. The temperature-dependent absorption coefficient is (see e.g.,

Table 1
Statistical Weights $g_{j_1 j_2}^{\epsilon}(f_p)$ for Different Combinations of Para- and Ortho- H_2 and Different Symmetries ϵ

j_1	j_2	ϵ	$g_{j_1 j_2}^{\epsilon}(f_p)$
even	even	+	f_p^2
even	even	−	0
odd	odd	+	$\frac{2}{3}(1-f_p)^2$
odd	odd	−	$\frac{1}{3}(1-f_p)^2$
even/odd	odd/even	...	$f_p(1-f_p)$

Karman et al. 2015):

$$\begin{aligned} \frac{\alpha(\nu, T)}{\rho^2} = & \sum_{E_{k'}^J > E_k^J} \frac{4\pi^3}{hc} \nu_{k'k}^{JJ'} \left(1 - \exp\left(-\frac{E_{k'}^J - E_k^J}{k_B T}\right) \right) \\ & \times \frac{h^3}{(2\pi m k_B T)^{3/2}} g_{j_1 j_2}^{\epsilon}(f_p) \\ & \times \exp\left(-\frac{E_k^J - E_{\text{asympt}}}{k_B T}\right) |M_{kk'}^{JJ'}|^2 \\ & \times \left(\frac{1}{w} - \frac{\max(\nu - \nu_{k'k}^{JJ'}, \nu_{k'k}^{JJ'} - \nu)}{w^2} \right), \end{aligned} \quad (7)$$

where ν is the wavenumber of the radiation in cm^{-1} and $\nu_{k'k}^{JJ'} = \frac{E_{k'}^J - E_k^J}{hc}$ is the transition wavenumber. E_{asympt} is the lowest asymptotic energy when the two hydrogen molecules are separated, i.e., for the case of one ortho- and one para-hydrogen $\frac{E_{\text{asympt}}}{hc} = \frac{E_1^{\text{mol}}}{hc} \approx 118.5 \text{ cm}^{-1}$. The last equation in parentheses in Equation (7) produces a triangular line profile of width w . The fraction of para- H_2 in the gas is f_p , which is 1, 0.5, 0.25 for pure para- H_2 , equilibrium- H_2 at 77 K, and normal H_2 , respectively. Those are the cases considered in the comparison with laboratory measurements in Section 2. The statistical weight g is given in Table 1. The matrix elements of the dipole moment is:

$$\begin{aligned} M_{kk'}^{JJ'} = & \sum_{\beta} \sum_{\beta'} \sum_{\alpha} \sum_{\lambda_1 \lambda_2 \lambda_L} F_{\beta k}^J(R_{\alpha}) A_{\lambda_1 \lambda_2 \lambda_L}(R_{\alpha}) \\ & \times F_{\beta' k'}^{J'}(R_{\alpha}) d_{\lambda_1 \lambda_2 \lambda_L}^{\beta J \beta' J'}, \end{aligned} \quad (8)$$

where the coefficient $d_{\lambda_1 \lambda_2 \lambda_L}^{\beta J \beta' J'}$ is given in Gustafsson et al. (2003). Note that the coefficient $d_{\lambda_1 \lambda_2 \lambda_L}^{\beta J \beta' J'}$ includes a factor $1/\sqrt{3}$, which would otherwise have appeared as $1/3$ in Equation (7). The spherical dipole components $A_{\lambda_1 \lambda_2 \lambda_L}$ come from the expansion of the electric dipole moment:

$$\begin{aligned} \mu_z(\hat{\mathbf{r}}_1, \hat{\mathbf{r}}_2, \mathbf{R}) = & \frac{(4\pi)^{3/2}}{\sqrt{3}} \sum_{\lambda_1 \lambda_2 \lambda_L} A_{\lambda_1 \lambda_2 \lambda_L}(R) \\ & \times Y_{\lambda_1 \lambda_2 \lambda_L}^{10}(\hat{\mathbf{r}}_1, \hat{\mathbf{r}}_2, \hat{\mathbf{R}}), \end{aligned} \quad (9)$$

where only the z -component has to be considered because the z -direction defines the angular momentum quantization axis in a space fixed frame of reference (Julienne 1982).

For the case of dimers consisting of two identical molecules (para–para or ortho–ortho) the wavefunctions have to be symmetrized. The symmetry parameter ϵ is + and − for symmetric and antisymmetric wavefunctions, respectively. Two of the formulas above have to be modified accordingly. In

Equation (6) the coefficient $e_{\gamma_1\gamma_2\gamma}$ has to be replaced by its ϵ -dependent version, and the same goes for $d_{\lambda_1\lambda_2\lambda_L}$ in Equation (8). The ϵ -dependent coefficients are given in the appendix of Gustafsson et al. (2003). Finally, the dipole selection rules have to be obeyed for all transitions included in the calculation of the absorption coefficient according to Equations (7) and (8). These are as follows:

1. Total angular momentum: $J' = J; J \pm 1$.
2. j_i and j'_i are both even or both odd for $i = 1$ or 2 .
3. Parity must change, implying that l changes from odd to even or vice versa.
4. In the case of identical molecules the symmetry, ϵ , is conserved.

ORCID iDs

Leigh N. Fletcher  <https://orcid.org/0000-0001-5834-9588>

References

- Anderson, E., Bai, Z., Bischof, C., et al. 1999, LAPACK Users' Guide (3rd ed.; Philadelphia, PA: SIAM)
- Birnbaum, G. 1978, *JQSRT*, **19**, 51
- Borysow, A., & Frommhold, L. 1986, *ApJ*, **304**, 849
- Borysow, A., & Frommhold, L. 1987, *ApJ*, **318**, 940
- Borysow, J., Frommhold, L., & Birnbaum, G. 1988, *ApJ*, **326**, 509
- Borysow, J., Trafton, L., Frommhold, L., & Birnbaum, G. 1985, *ApJ*, **296**, 644
- Campargue, A., Kass, S., Pachucki, K., & Komasa, J. 2012, *PCCP*, **14**, 802
- Carlson, B. E., Lacis, A. A., & Rossow, W. B. 1992, *ApJ*, **393**, 357
- Colbert, D. T., & Miller, W. H. 1992, *JChPh*, **96**, 1982
- Conrath, B. J., & Gautier, D. 2000, *Icar*, **144**, 124
- Conrath, B. J., Gierasch, P. J., & Ustinov, E. A. 1998, *Icar*, **135**, 501
- Fakhardji, W., & Gustafsson, M. 2017, *JPhCS*, **810**, 012031
- Flasar, F. M., Kunde, V. G., Abbas, M. M., et al. 2004, *SSRv*, **115**, 169
- Fletcher, L. N., de Pater, I., Orton, G. S., et al. 2014, *Icar*, **231**, 146
- Fletcher, L. N., de Pater, I., Reach, W. T., et al. 2017, *Icar*, **286**, 223
- Fletcher, L. N., Hesman, B. E., Achterberg, R. K., et al. 2012, *Icar*, **221**, 560
- Fletcher, L. N., Irwin, P. G. J., Achterberg, R. K., Orton, G. S., & Flasar, F. M. 2016, *Icar*, **264**, 137
- Fletcher, L. N., Orton, G. S., Teanby, N. A., & Irwin, P. G. J. 2009, *Icar*, **202**, 543
- Frommhold, L., Samuelson, R., & Birnbaum, G. 1984, *ApJL*, **283**, L79
- Goody, R. M., & Yung, Y. L. 1989, in *Atmospheric Radiation: Theoretical Basis*, ed. R. M. Goody & Y. L. Yung (2nd ed.; New York: Oxford Univ. Press)
- Green, S. 1975, *JChPh*, **62**, 2271
- Gustafsson, M. 2017, *J. Phys. Conf. Ser.*, **810**, 012017
- Gustafsson, M., Frommhold, L., Bailly, D., Bouanich, J.-P., & Brodbeck, C. 2003, *JChPh*, **119**, 12264
- Hartmann, J.-M., Boulet, C., & Jacquemart, D. 2011, *JChPh*, **134**, 094316
- Houck, J. R., Roellig, T. L., van Cleve, J., et al. 2004, *ApJS*, **154**, 18
- Irwin, P., Teanby, N., de Kok, R., et al. 2008, *JQSRT*, **109**, 1136
- Julienne, P. S. 1982, *PhRvA*, **26**, 3299
- Karman, T., van der Avoird, A., & Groenenboom, G. C. 2015, *JChPh*, **142**, 084305
- Kim, S. J., Trafton, L. M., Geballe, T. R., & Slanina, Z. 1995, *Icar*, **113**, 217
- Korn, G. A., & Korn, T. M. 1968, *Mathematical Handbook for Scientists and Engineers* (2nd ed.; New York: McGraw-Hill)
- McKellar, A. R. W. 1984, *CaJPh*, **62**, 760
- McKellar, A. R. W. 1988, *ApJL*, **326**, L75
- McKellar, A. R. W. 1990, *JChPh*, **92**, 3261
- McKellar, A. R. W., & Schaefer, J. 1991, *JChPh*, **95**, 3081
- Meyer, W., Borysow, A., & Frommhold, L. 1989, *PhRvA*, **40**, 6931
- Meyer, W., Frommhold, L., & Birnbaum, G. 1989, *PhRvA*, **39**, 2434
- Orton, G. S., Fletcher, L. N., Encenaz, T., et al. 2015, *Icar*, **260**, 94
- Orton, G. S., Fletcher, L. N., Moses, J. I., et al. 2014a, *Icar*, **243**, 494
- Orton, G. S., Gustafsson, M., Burgdorf, M., & Meadows, V. 2007, *Icar*, **189**, 544
- Orton, G. S., Moses, J. I., Fletcher, L. N., et al. 2014b, *Icar*, **243**, 471
- Reuter, D. C., & Sirota, J. M. 1994, *ApJL*, **428**, L77
- Richard, C., Gordon, I. E., Rothman, L. S., et al. 2012, *JQSRT*, **113**, 1276
- Rodgers, C. D. 2000, *Inverse Methods for Atmospheric Remote Sounding: Theory and Practice* (Singapore: World Scientific)
- Rothman, L. S., Gordon, I. E., Babikov, Y., et al. 2013, *JQSRT*, **130**, 4
- Schaefer, J. 1987, *A&A*, **182**, L40
- Schäfer, J., & Köhler, W. E. 1989, *ZPhyD*, **13**, 217
- Stoicheff, B. P. 1957, *CaJPh*, **35**, 730
- Trafton, L. M., Kim, S. J., Geballe, T. R., & Miller, S. 1997, *Icar*, **130**, 544
- Wells, M., Pel, J.-W., Glaspe, A., et al. 2015, *PASP*, **127**, 646